Astronomy
&
Astrophysics

X-ray spectroscopy of the Hertzsprung-gap giant star 31 Com, observed with XMM-Newton[⋆]

L. Scelsi[1], A. Maggio[2], G. Peres[1], and Ph. Gondoin[3]

[1] Dipartimento di Scienze Fisiche ed Astronomiche, Sezione di Astronomia, Università di Palermo, Piazza del Parlamento 1, 90134 Palermo, Italy

[2] INAF – Osservatorio Astronomico di Palermo, Piazza del Parlamento 1, 90134 Palermo, Italy

[3] Research and Scientific Support Department, ESA-ESTEC, Noordwijk, The Netherlands

Abstract. We have analysed the *XMM-Newton* X-ray spectra of the yellow giant 31 Com with the aim of deriving information on the coronal structures of this archetypical Hertzsprung-gap star. To determine the emission measure distribution vs. temperature, $EM(T)$, and the elemental abundances of the coronal plasma, with an accurate line-based approach, we have developed a new method for simple and accurate line measurements, based on rebinning and co-adding the two RGS spectra. We have reconstructed the $EM(T)$ independently with both APED and CHIANTI atomic databases in order to investigate possible differences in the final outcome of the analysis, and we have obtained consistent results. The derived emission measure distribution has a well defined peak at $T \sim 10^7$ K and a significant amount of plasma at higher temperatures; there is also evidence for plasma at temperatures below $\sim 10^{6.5}$ K, with a mean electron density of $\sim 3 \times 10^{10}$ cm^{-3}, as inferred from the line ratio of the O VII triplet. We have made a global fitting of the EPIC spectra, using multi-component isothermal (3-T) model, and then compared the results with the $EM(T)$, looking for a consistent multi-temperature description of both the RGS and EPIC spectra, over the whole spectral range. While the $EM(T)$ and the 3-T models individually provide a good description of the data set on which they are based, none of them describes adequately the data of all the other instruments; the disagreements may be related, at least in part, to cross-calibration problems. Finally, we have used the $EM(T)$ to derive information about the properties of the coronal structures. Our results indicate that the corona of 31 Com is dominated by a class of magnetic loops with peak temperature $\sim 10^7$ K and apparently more isothermal than the solar ones.

Key words. X-rays: stars – techniques: spectroscopic – stars: activity – stars: coronae – stars: individual: 31 Com

1. Introduction

Spatially resolved observations of the solar corona provide us with some hints to interpret the X-ray emission from unresolved late-type stars, in terms of coronal magnetic loops confining an optically thin plasma. On the other hand, the results of past and present analyses of stellar X-ray spectra suggest that in many cases the coronae can not be described simply as a scaled-up version of the solar one; indeed, there is increasing evidence that the coronae of very active stars, with emission levels up to 10^4 times that of the Sun, are hotter and more isothermal than coronae of solar-type stars (Guedel 1997; Drake et al. 2000; Sanz-Forcada et al. 2002).

One of the central issues in the physics of outer stellar atmospheres is how coronal structures in high-luminosity late-type stars compare with the solar-type coronal loops. Most of the previous analyses of low- or medium-resolution spectra

have been performed using simple models with a few isothermal components, which make an interpretation of the observed X-ray emission in terms of coronal structures difficult. Line spectroscopy, finally achievable with the instruments onboard the satellites *EUVE*, *XMM* and *Chandra*, allows us to measure the flux of individual emission lines to derive the emission measure distribution vs. temperature of the coronal plasma, to estimate density and pressure from spectroscopic diagnostics and, more generally, to study the characteristics of the coronal plasma in greater detail than before. These information can be employed to characterize the coronal structures and loop populations using techniques developed for this purposes by Peres et al. (2001) and recently employed for modeling the corona of Capella (Argiroffi et al. 2003).

High X-ray luminosity yellow giants are especially interesting because (i) their magnetic dynamo is probably very "young" (Pizzolato et al. 2000), because in stars with $M > 1.5\,M_\odot$ it is triggered by the onset of efficient subphotospheric convection occuring in the phase of crossing the Hertzsprung-gap; (ii) surface gravity is significantly lower than in dwarf stars, with the implication that pressure scale heights

Send offprint requests to: L. Scelsi,
e-mail: `scelsi@oapa.astropa.unipa.it`

⋆ Table 3 and Appendix A are only available in electronic form at `http://www.edpsciences.org`

are larger and hence coronae may be significantly more extended than in solar-type stars; (iii) different interpretative models have been suggested for them: hot but otherwise solar-like coronal structures, or large-scale magnetospheres (Ayres et al. 1998).

31 Com (HD 111812) is a good target for such a kind of studies because it is a single star with high X-ray flux at Earth, due to its high X-ray luminosity ($L_X \sim 10^{31}$ erg s^{-1}) and its distance $d \sim 94$ pc (parallax = 10.62 ± 0.90 mas, Perryman et al. 1997). It is an evolved G0III star in the Hertzsprung-gap, having a mass of $\sim 3 \, M_\odot$ and estimated radius of $\sim 9.3 \, R_\odot$ (Pizzolato et al. 2000). 31 Com is also a rapid rotator, its projected velocity being $v \sin i \sim 66$ km s^{-1} (de Medeiros & Mayor 1999). This target has been observed many times with past generation instrumentation: *Einstein* (Maggio et al. 1990), *ROSAT* (Pizzolato et al. 2000), *ASCA* (Ueda et al. 2001), *EUVE* (Ayres et al. 1998). Here we present results of an *XMM-Newton* observation, which allowed us to obtain simultaneously medium-resolution EPIC CCD spectra and high-resolution RGS spectra of this source. One of the issues addressed in this paper is whether a coherent and consistent description can be derived from these different data sets, which can be analyzed with different methods. In fact, while multi-T models are still adequate to perform global fitting of EPIC CCD spectra, the RGS data call for a more detailed and accurate analysis based on the identification and measurement of individual emission lines. A second issue related to the line-based analysis of the emission line spectra is whether different atomic databases yield consistent results. In particular, the two most up to date public databases currently available are APED (Smith et al. 2001) and CHIANTI (Dere et al. 1997; Young et al. 1998; Landi et al. 1999; Dere et al. 2001). The former includes in part the CHIANTI data, and possibly it is the most complete database because transitions from high-n states are also included. However the analysis of either *Chandra* or *XMM-Newton* grating spectra is usually performed with only one of the two databases, and it is not sufficiently clear whether the results of such analyses can be compared.

Summing up, in this paper we will address both the scientific issue of inferring the properties of coronal structures in high-luminosity coronal sources and issues related to the data analysis. In Sect. 2 we report the details of the observation analyzed here; in Sect. 3 we describe the data reduction and the methods used for the analyses of EPIC and RGS spectra; we show the results in Sect. 4 and discuss them in Sect. 5. Finally, we draw our conclusions in Sect. 6.

2. Observations

31 Com was observed on January 9, 2001, as part of the first *XMM-Newton* Guest Observation phase (PI: Ph. Gondoin). The satellite is equipped with three X-ray telescopes (Gondoin et al. 2000) and carries five detectors: two *European Photon Imaging Cameras* with MOS CCDs (EPIC MOS, Turner et al. 2001), one with pn CCDs (EPIC pn, Strüder et al. 2001), and two *Reflection Grating Spectrometers* (RGS, den Herder et al. 2001). The non dispersive EPIC cameras provide spectral resolution $R = E/\Delta E \sim 20-50$ in the range 0.1–10 keV;

Table 1. Log of the *XMM-Newton* observation.

Instrument	Exposure time (ks)	Mode of data acquisition	Filter	Count-rate[a] (s^{-1})
pn	32.2	Full Frame	thick	1.45
MOS1	37.9	Large Window	thick	0.90
MOS2	37.9	Large Window	thick	0.92
RGS1	39.6	Spectroscopy	–	0.11
RGS2	38.5	Spectroscopy	–	0.16

[a] In the 1.2–62 Å (0.2–10 keV) band for pn and the MOS and in the 5–38 Å (0.32–2.5 keV) band for the RGS.

the RGS spectrometers cover the wavelength range 5–38 Å (0.32–2.5 keV) with resolution $R \sim 70-500$. For the observation analyzed here, data are available from all the X-ray detectors on board *XMM*. Table 1 reports details on the instrument configuration and on the observation (exposure time, mode of data acquisition, filter and the source count-rates in each extraction region). RGS1 data are affected by the lack of CCD 7, corresponding to the spectral region containing the Ne IX triplet, while the RGS2 spectrum lacks the region of the O VII triplet, due to the failure of CCD 4.

3. Data analysis

The data were reduced using SAS version 5.3.3 together with the calibration files available at the time of the analysis (summer 2002). The pn and MOS responses were generated with the SAS rmfgen and arfgen tasks. Second order RGS spectra have not been considered, because of their low statistics.

We have selected Good Time Intervals by removing a few short time intervals (~ 2 ks in total) which show the presence of presumable proton flares in the X-ray light curve of the background extracted from CCD 9 of the RGS (the excluded intervals are those with background count rate >0.1 cts s^{-1}).

EPIC spectra were analyzed with XSPEC using multi-component thermal models based on the Astrophysical Plasma Emission Database (APED/ATOMDB V1.2).

For line-based analysis of RGS spectra, we employed the software package PINTofALE (Kashyap & Drake 2000) and, in part, also XSPEC and the MIT/CXC *Interactive Spectral Interpretation System* (ISIS, Houck & Denicola 2000). We have adopted both APED/ATOMDB (V1.2) and the CHIANTI (V3) database, together with the Mazzotta et al. (1998) ionization equilibrium, for line identification and the emission measure analysis.

Note that the RGS Line Spread Functions are characterized by extended wings which often make it impossible to determine the true source continuum emission from the data. We have used the multi-T model best-fitting the EPIC pn spectrum to evaluate the initial guess of the continuum level for the line measurements; it represents a good starting point in the iterative procedure aimed at obtaining the emission measure distribution vs. temperature, as described in Sect. 3.2.
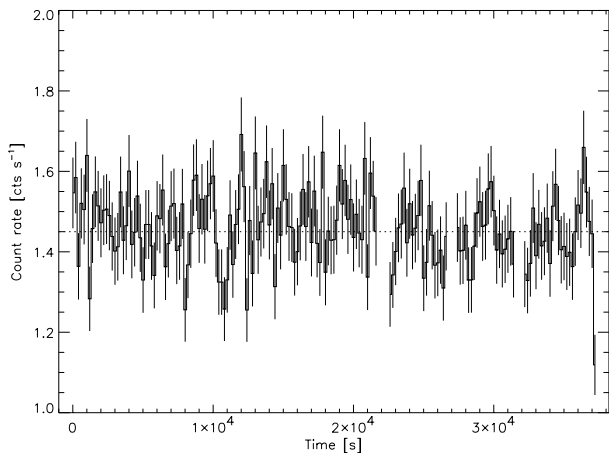
Fig. 1. pn light curve in the 1.2−62 Å (0.2−10 keV) band, with time bins of 200 s. The gaps correspond to the time of high background emission, excluded from the analysis. The dotted line marks the mean count rate of the source during the observation. The analysis shows that no significant variability is present.

3.1. EPIC data

For MOS data, source photons have been extracted from a circular region (60″ radius), and background events from an annular region around the source and inside the central CCD.

The EPIC pn data were affected by pile-up and we avoided this effect by removing the central part of the Point Spread Function, i.e. extracting source counts from an annulus (7.5″−50″ radii), within CCD 4; background photons were obtained from the rest of CCD 4, excluding the source and its out-of-time events.

The pn background-subtracted light curve of 31 Com, with time bins of 200 s, is shown in Fig. 1 and it is consistent with the null hypothesis of a constant emission ($\chi^2_\nu = 1.03$, with 175 d.o.f.). We have verified that the same result follows with a 500 s time binning.

We have used a global fitting to analyze the EPIC spectra (Fig. 2). The instrumental response of the two MOS detectors are thought to be very similar so, at first, their data were fitted simultaneously. Yet, the result of the fitting showed evidence for residual cross-calibration discrepancies between the two instruments, the major problems being possibly ascribed to the MOS1; details about this subject are reported in Appendix B, where we also discuss cross-calibration inconsistencies between the MOS1 and the RGS spectrometers. We eventually performed global fittings of each of the MOS spectra separately.

The model chosen to fit the EPIC spectra is an absorbed, optically-thin, three components thermal plasma; we added a fourth component to investigate whether it is possible to obtain a better description of the data, but we found no improvement. The free abundances of the model are those of O, Ne, Mg, Si, S, Fe and Ni, whose line complexes are strong and clearly detected in EPIC spectra (but also in RGS spectra). On the contrary, the abundances of C, N, Al, Ar and Ca were tied to that of Fe because, when left free to vary, their best-fit values were
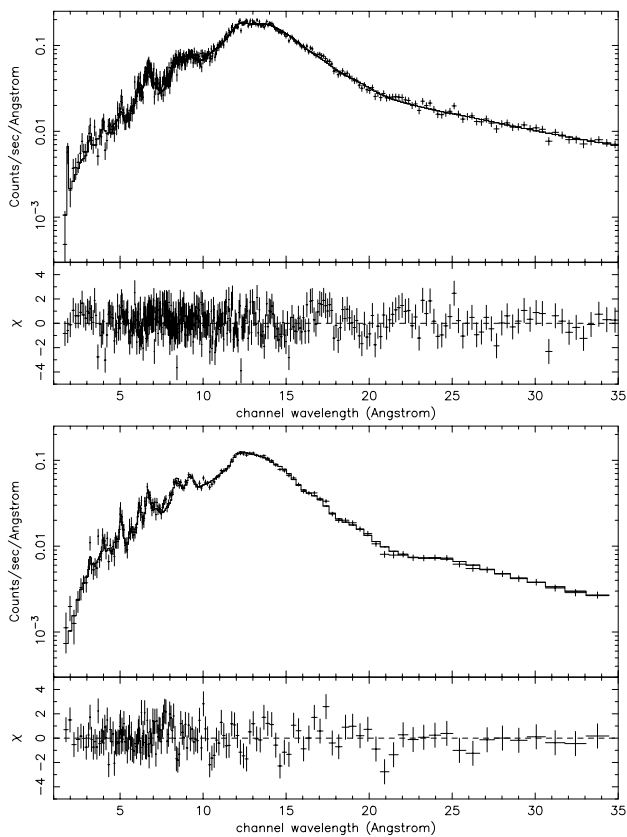

Fig. 2. EPIC pn (upper) and MOS2 (lower) spectra, with their best-fit model spectra (the parameters of the models are listed in Table 2).

ill-constrained. This choice allowed us to limit the number of free parameters to 13.

3.2. RGS

The analysis of RGS spectra consisted of the following steps: line identification, flux measurements, line screening, reconstruction of the emission measure distribution vs. temperature, $EM(T)$, and simultaneous determination of elemental abundances, followed by estimate of metallicity and check of the solution.

We have combined the RGS1 and RGS2 spectra (Fig. 3) in order to increase the signal-to-noise ratio and, consequently, to make line identification easier and to get more accurate flux measurements. Both RGS spectra are defined, by default, onto 3400 wavelength channels, whose width ranges from 0.007 to 0.014 Å. However, the wavelength grids of RGS1 and RGS2 do not coincide, hence their spectra cannot be summed directly. The approach we adopted to measure line fluxes allowed us to get a self-consistent solution in terms of $EM(T)$ and a set of abundances, i.e. a solution which reproduces the measured fluxes and the continuum level assumed for flux measurements, and which gives a sufficiently accurate description of the RGS spectra of 31 Com, within the limitations of the atomic database (Fig. 4).

For the identification of the strongest emission lines and the measurement of their fluxes, we have co-added the background-subtracted RGS1 and RGS2 spectra, after

Table 2. Best-fit models of the EPIC data (in the 1.5–41 Å band), with 90% statistical confidence ranges computed for one interesting parameter at a time; nominal errors on T_i and EM_i are at the 10% level. Element abundances are relative to the solar ones (Grevesse et al. 1992). Mean temperatures are calculated as $< T > = \sum_{i=1}^{3} EM_i T_i / \sum_{i=1}^{3} EM_i$.

	pn	MOS2
$\log T_{1,2,3}$ (K)	6.44, 6.92, 7.28	6.70, 6.95, 7.25
$\log EM_{1,2,3}$ (cm^{-3})	52.6, 53.1, 53.0	52.5, 53.4, 53.2
$\log < T >$ (K)	7.06	7.07
C[a]	0.38	0.22
O	0.58 ± 0.03	0.37 ± 0.05
Ne	2.35 ± 0.14	0.58 ± 0.09
Mg	1.95 ± 0.13	0.96 ± 0.08
Si	1.23 ± 0.11	0.69 ± 0.06
S	0.58 ± 0.20	0.60 ± 0.13
Fe	1.54 ± 0.02	0.87 ± 0.02
Ni	4.1 ± 0.3	1.4 ± 0.2
N_H (cm^{-2})[b]	10^{18}	10^{18}
χ_ν^2/d.o.f.	1.1/367	1.2/150

[a] Fixed to 0.25 times the iron abundance (see text for explanations).
[b] Fixed (see text).

rebinning each of them on the same grid, and we have adopted a Lorentzian line profile. We give further details on the new methodology we have developed in Appendix A, where we also demonstrate that it provides total line fluxes consistent with those obtained by fitting the line profiles in the individual RGS spectra with the detailed Line Spread Function; on the other hand, our approach allows to work on data with higher S/N ratio.

We based the subsequent *EM* reconstruction on a set of selected lines, among the identified ones, whose flux measurements and theoretical emissivities were reliable. In particular, we rejected lines with low signal-to-noise ratio or highly blended with others, lines lying in proximity of bad pixels and inter-chip-gaps, lines whose fluxes are not compatible with those of others lines of the same ion, according to theoretical estimates (possibly indicating large uncertainty in the relevant emissivity curves). Finally, we also excluded density-sensitive lines. In this way, the equation relating the differential emission measure ($dem(T) = n_e^2 \, dV/d \log T$) of an optically thin plasma with the flux at Earth F_{if} of an ion transition from the level i to the level f contains only temperature-dependent quantities:

$$F_{if} = e^{-\sigma_{abs} N_H} \frac{h\nu_{if}}{4\pi d^2} A_Z \int_T G_{if}(T) \, dem(T) \, d \log T \quad (1)$$

where $e^{-\sigma_{abs} N_H}$ is the interstellar absorption coefficient, ν_{if} is the line frequency, d is the distance of the star, A_Z is the abundance of the element Z and $G_{if}(T)$ is the emissivity function of the transition. We used the Markov-Chain Monte Carlo (MCMC) method by Kashyap & Drake (1998) which yields a volume emission measure distribution, rather than the continuous function $dem(T)$, owing to the discretization of Eq. (1).

The distribution, $EM(T_k) = dem(T_k) \Delta \log T$, is defined over a pre-selected temperature grid, in the range $\log T = 6.0$–7.7 and with $\Delta \log T = 0.1$.

The MCMC method is based on the random sampling of the values $EM(T_k)$, in order to maximize the probability:

$$P(F_1, ..., F_N) \propto \exp\left[- \sum_{j=1}^{N} \frac{(F_j - F_j^{pred})^2}{2 \sigma_j^2} \right] \quad (2)$$

where F_j, σ_j and F_j^{pred} are, respectively, the measured flux of the jth selected line, its error and the flux predicted according to Eq. (1). This algorithm can assign statistical error bars on the values $EM(T_k)$ that are frequently sampled; since the $EM(T_k)$ value to be varied at each iteration is chosen on the basis of a probability distribution of the relevant T_k, and this distribution is defined as proportional to the sum of the normalized emissivity functions of all the selected lines, the value $EM(T_k)$ will be constrained if we have a sufficient number of selected lines which form around the temperature T_k.

The method also provides estimates of element abundances, relative to iron, with their statistical uncertainties.

We checked the solution obtained with the MCMC in three steps. First, we compared the line fluxes predicted according to our solution with the measured ones; we then checked the reliability of the "cool" and "hot" tails of the $EM(T)$ and, at the same time, estimated the iron abundance, by scaling the emission measure distribution accounting for various metallicities and by comparing the synthetic spectrum with the observed one, in selected spectral regions free of overlapping emission lines (these are the regions at $\lambda > 20$ Å in the RGS spectrum and at $\lambda < 4$ Å in EPIC spectra). We finally checked the consistency between the continuum level assumed for flux measurements and the predicted continuum. In this analysis we have found agreement between the observed and predicted fluxes, indicating a substantially correct shape of the $EM(T)$, at least in the central part of the temperature range where it is formally constrained, and we have verified a good agreement between the assumed and the predicted levels of the continuum even in the wavelength range 10–17 Å, where the large number of blends does not allow us to estimate it directly. Hence, checking the solution was successful already after one iteration of the whole procedure, in both the cases where we used the APED or the CHIANTI database.

4. Results

4.1. EPIC

Figure 2 shows the pn and MOS2 spectra with their best-fit models. In these spectra we can clearly detect the line complexes of Mg XI-XII (~8.5–9.3 Å), Si XIII-XIV (~6–6.8 Å) and S XV (~5 Å), while the complexes of Ar XVII (~4 Å) and Ca XIX (~3.2 Å) are only just detectable. The pn spectrum also shows emission from the Fe XXV 1.85 Å line, indicating the presence of a hot corona (this ion forms at ~$10^{7.8}$ K).

The fittings were performed in the 1.5–41 Å (0.3–8 keV) interval; we used the result of the EM analysis to fix the coronal ratio between the C and Fe abundances equal to 0.25 times the
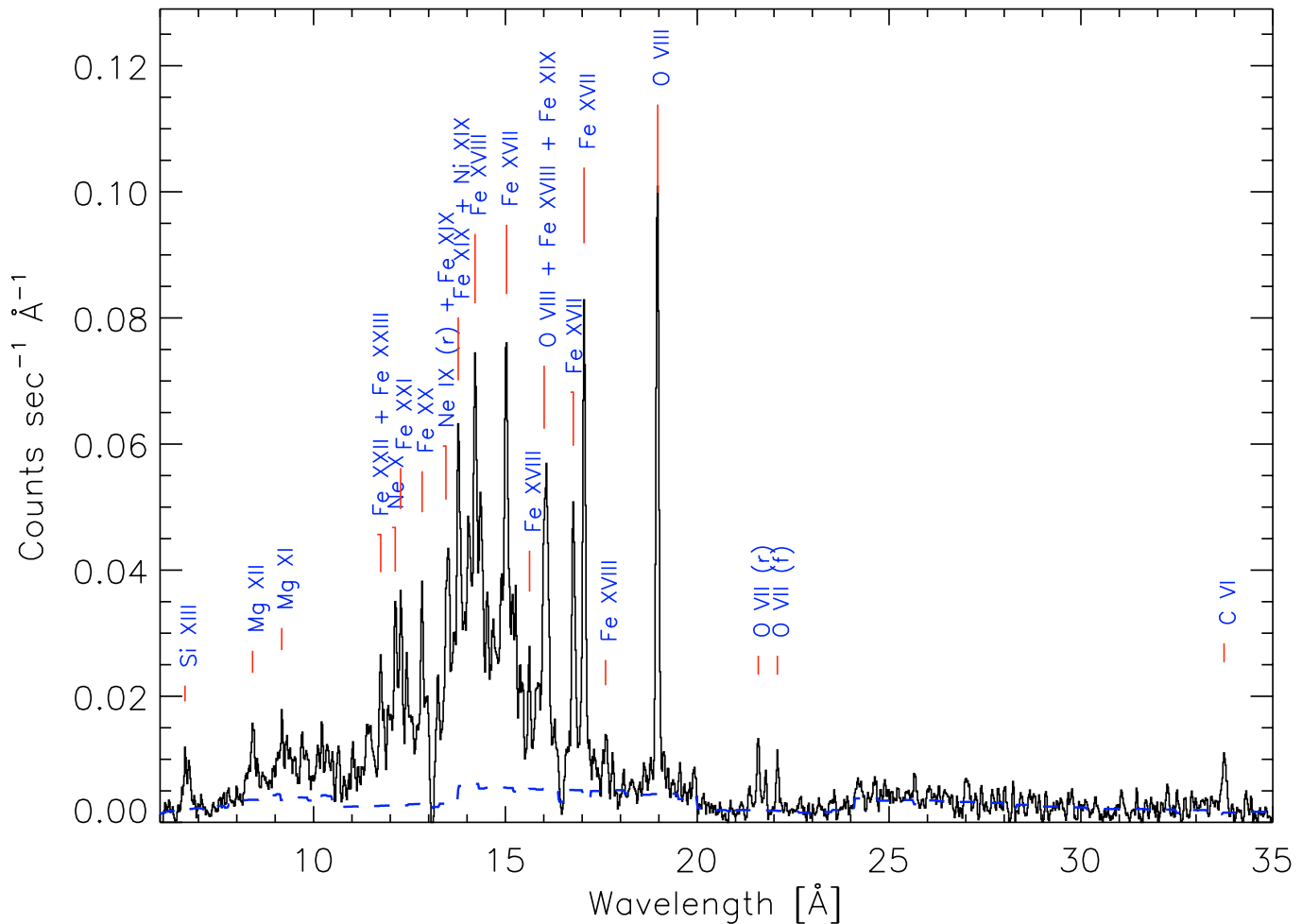
Fig. 3. Co-added RGS spectrum of 31 Com with the identification of the most prominent lines; the bin size is 0.02 Å. The dashed line represents the continuum emission of the source, derived from the final $EM(T)$ model; note that it is impossible to estimate the continuum from the data in the 10–17 Å range.

solar one (Grevesse et al. 1992), while for N, Al, Ar and Ca the abundances were linked to that of Fe assuming the same ratios as the solar case (see the criteria mentioned in Sect. 3.1).

In Table 2 we list the best-fit parameters for the pn and MOS2 data only (the simultaneous fitting of MOS spectra as well as the description of the MOS1 spectrum alone provided by the 3-T model were not statistically acceptable; they will be partially discussed in Appendix B). Note the large emission measures ($1-2 \times 10^{53}$ cm^{-3}) obtained for the high temperature components ($T \sim 10-20$ MK). Note also that we have fixed the interstellar absorption at the value $N_H = 10^{18}$ cm^{-2} measured by Piskunov et al. (1997). If left free to vary, the best fit value for N_H would be $\sim 3 \times 10^{20}$ cm^{-2}, an order of magnitude higher than that estimated assuming a mean hydrogen density ~ 0.1 cm^{-3} (Paresce 1984).

4.2. RGS

4.2.1. Line identification and selection

In the RGS1+RGS2 spectrum of 31 Com (Fig. 3), we have identified about 80 lines from Fe XVII–XXIV ions, from

He–like and H–like O VII-VIII, Ne IX-X, Mg XI-XII, Si XIII and C VI ions, and from Ni XIX-XX. These lines are listed in Table 3, where we made the effort to match the atomic transitions in the CHIANTI database with those in APED, based on the spectroscopic term, whenever possible[1]. The total number of listed APED transitions is 219, while in the case of CHIANTI only 135 transitions have been identified; it is worth noting that there are about 20 spectral features for which significantly or totally different identifications result from the two databases. In principle, these differences might yield different outcomes of the emission measure analyses performed with APED and CHIANTI, but we will show in the following that consistent results can be obtained with our approach.

The lines used for the *EM* reconstruction with APED or CHIANTI are marked with "a" or "c", respectively. Note the few lines making exception to the selection criteria reported in Sect. 3.2: the resonance line of the Ne IX triplet was selected although blended with the Fe XIX lines at $\sim$13.52 Å, because it is the only one with a peak of emissivity at $\log T \sim$ 6.6 and helps to extend the emission measure distribution to

---

[1] Note that some of the APED lines are defined in the j–j coupling formalism, while CHIANTI always uses the L-S coupling expression.
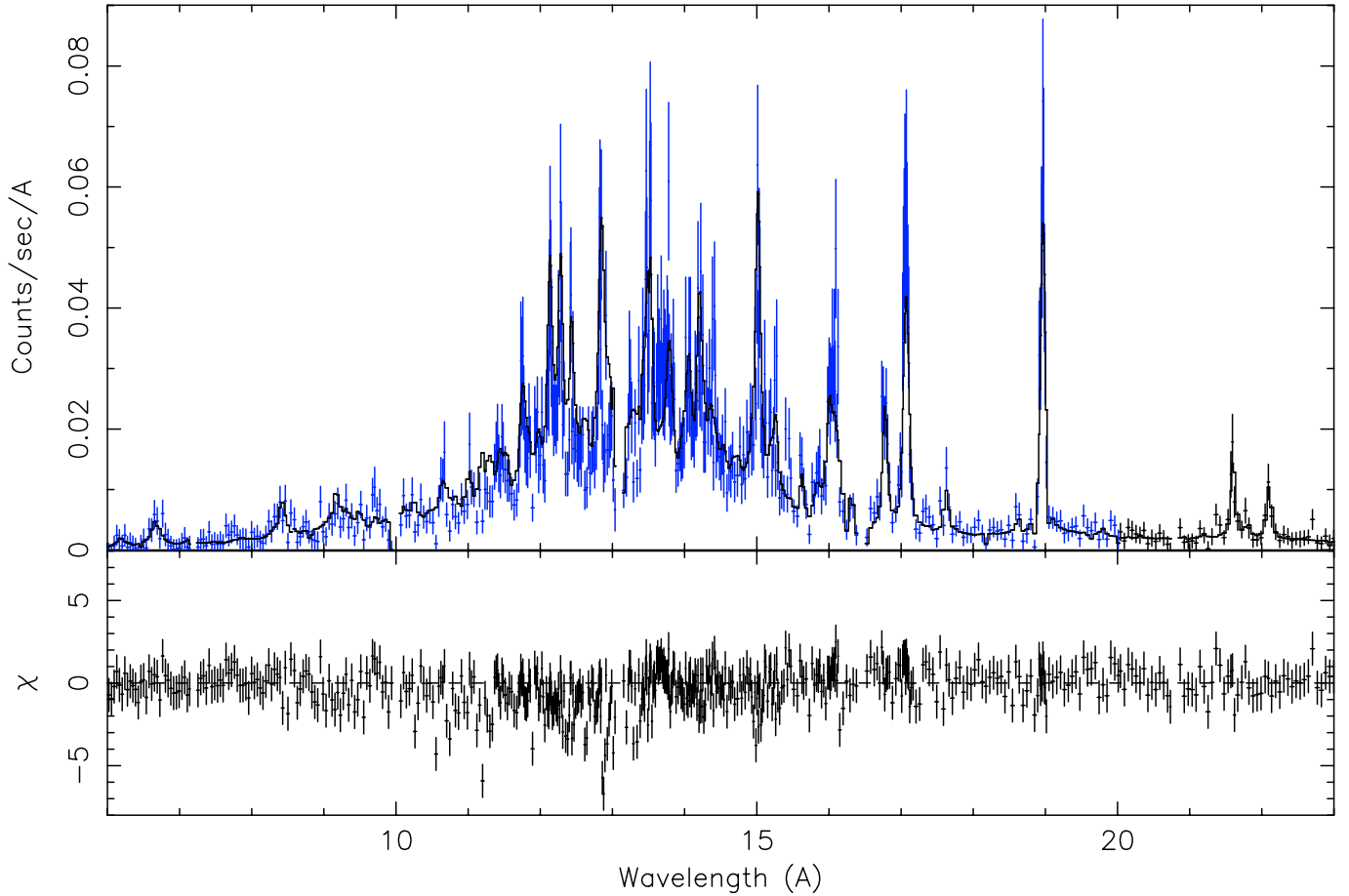
Fig. 4. The "APED" model spectrum derived from the $EM(T)$ is compared with the original RGS1 and RGS2 spectra.

lower temperatures, after the initial reconstruction using the Fe lines only; the weak Fe XXIII 8.31 Å line has been included in the APED selection because it is consistent with the other Fe XXIII–XXIV lines and helps in determining the $EM(T)$ at high temperature ($\log T \sim 7.2$); we have also used the strong Fe XVII 17.05 Å line, which lies in proximity of an inter-chip gap, as its flux agrees with the value obtained by the alternative method described in Appendix A.

4.2.2. Emission measure distribution and abundances

The emission measure distributions derived with the APED and CHIANTI databases are shown in Fig. 5; they look very similar and share several notable features. Considering first the constrained part (i.e. for which error bars could be derived) in common to both, $6.5 < \log T < 7.2$, we observe agreement within the error bars. Note also that the "CHIANTI" distribution resulted statistically constrained in a slightly larger range with respect to the "APED" solution, as a consequence of the smaller number (relative to the total) of lines which form at intermediate temperatures ($6.6 < \log T < 7.1$) in the "CHIANTI" selection with respect to the "APED" one. This caused a slightly different sampling for the $EM(T_k)$ values by the MCMC procedure in the two cases and hence a different set of constrained values.

The two distributions are sharply peaked at $\log T = 7$ and both show the presence of plasma both at temperatures lower than $10^{6.5}$ K and higher than $10^{7.2}$ K. Although we are not able to assign errors on these "cool" and "hot" tails of the $EM(T)$, they are rather reliable: in fact, the "cool" tail is needed to adequately describe the O VIII Ly α/ O VII ratios, while the "hot" tail is required by the Fe XXIII–XXIV lines measured in the RGS spectrum, as well as by the H–like and He–like complexes of S, Ca, Ar and Fe and the continuum visible at high energies in the EPIC spectra.

In Fig. 6 we compare the observed and predicted fluxes, most of which agree within a factor 2; yet, some problems relevant to the emissivities of Fe XVIII lines in the CHIANTI database are evident, as the fluxes of the selected Fe XVIII lines, which form at $\log T \sim 6.9$, are all underestimated, except the one at 14.20 Å. In the case of APED, we do not note such a systematic trend, and only two out of nine Fe XVIII lines, at 15.87 Å and 16.07 Å, are underestimated.

The elemental abundances obtained from both analyses are shown in Table 4 and they are all compatible each others; in both cases, we estimated an iron abundance in 1.4 ± 0.2 times the solar one. As an example, Fig. 7 shows the predicted continuum spectra for different metallicities superimposed to the observed spectrum, for the case of the analysis performed with APED.
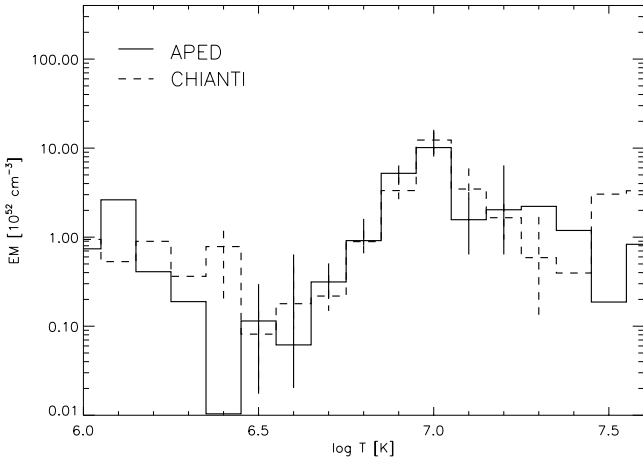
Fig. 5. Emission measure distributions reconstructed with the MCMC method and the APED (solid line) and CHIANTI (dashed line) databases.
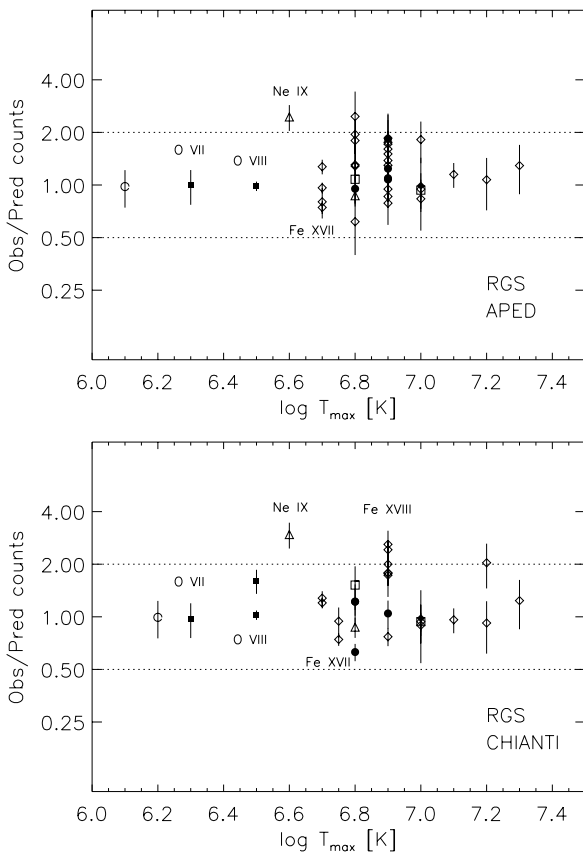
Table 4. Ratios between elemental and iron coronal abundances, relative to the solar photospheric ratios (Grevesse et al. 1992), derived from RGS data, using the APED and CHIANTI databases; errors are at 68% confidence level. For each element, the number of lines included in the *EM* reconstruction is also shown.

	APED	No. lines	CHIANTI	No. lines
C	$0.24^{+0.22}_{-0.07}$	1	$0.35^{+0.4}_{-0.12}$	1
O	$0.49^{+0.15}_{-0.08}$	2	$0.41^{+0.14}_{-0.06}$	3
Ne	$0.78^{+0.13}_{-0.3}$	2	$0.62^{+0.23}_{-0.08}$	2
Mg	$1.0^{+0.4}_{-0.3}$	2	$0.82^{+0.25}_{-0.14}$	2
Si	$0.9^{+0.9}_{-0.3}$	1	$0.85^{+1.0}_{-0.27}$	1
Fe	1	27	1	17
Ni	$3.5^{+2.1}_{-0.7}$	6	$4.6^{+1.1}_{-1.0}$	4
total lines		41		30

Fig. 6. Comparison between observed fluxes and the fluxes predicted with the APED (upper panel) and CHIANTI (lower panel) *EM(T)* models, for lines used in the *EM* reconstruction; Fe: open diamonds, Ne: triangles, Mg: open squares, Si: filled diamond, Ni: filled circles, O: filled squares, C: open circle.

4.2.3. Density and temperature diagnostic from the He–like O VII triplet

Though the wavelength range of the RGS includes the He–like triplets of the ions C V, N VI, O VII, Ne IX, Mg XI and Si XIII, we were able to analyze only the O VII triplet, the others
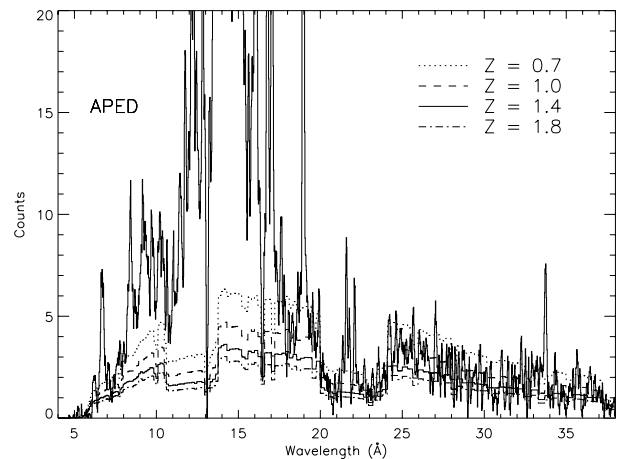

Fig. 7. Comparison between observed spectrum and continuum emission predicted with the *EM(T)* for different metallicities *Z*; we have used the APED database.

being either not detectable (C V and N VI), or too weak and only partially resolved (Mg XI and Si XIII) or highly blended with Fe XIX lines (Ne IX).

We determined the plasma electron density and temperature, averaged over the region where the triplet forms, from the ratios $R_d = f/i$ and $R_t = (i + f)/r$ respectively (Gabriel & Jordan 1969; Porquet et al. 2001), where f is the flux of the forbidden line, i of the intercombination line and r of the resonance line. Due to the low photon counting statistics (Table 3), the errors on these ratios are very large: we obtain $R_d = 2.0 \pm 1.4$ and $R_t = 0.94 \pm 0.36$, and hence we derive a mean plasma density of $n_e \sim 3 \times 10^{10}\,\mathrm{cm}^{-3}$ (with 68% confidence range $\sim 6 \times 10^9 – 2 \times 10^{11}\,\mathrm{cm}^{-3}$) and an average temperature of $T_e \sim 1.5^{+2.5}_{-0.7} \times 10^6$ K, using the theoretical curves by Smith et al. (2001). From the values of T_e and n_e we can estimate the average pressure relative to the region where the triplet forms: $P_e \sim 13\,\mathrm{dyn\,cm}^{-2}$, with an uncertainty range (extremes of the product $2n_e k_b T_e$) $\sim 1.5 – 220\,\mathrm{dyn\,cm}^{-2}$.
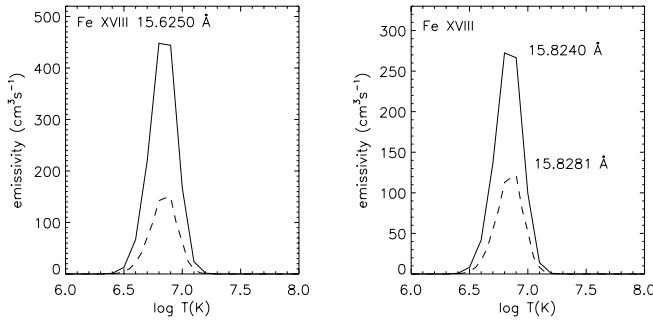
Fig. 8. Examples of differences between emissivity curves of the same transitions in the APED (solid line) and CHIANTI (dashed line) databases.

5. Discussion

5.1. APED vs. CHIANTI

We performed the two analyses with the APED and CHIANTI databases indipendently from each other, with the consequence that the sets of selected lines are not the same. This choice is motivated by the need of testing the overall effect of one database with respect to the other on the *EM* reconstruction. Although some ion transitions may be described with emissivity curves significantly different in the two databases (Fig. 8), we have found that the two *EM* solutions are compatible, as shown in Fig. 5 and in Table 4.

The reason of the robustness of our result is that the emission measure reconstruction is based on a set of several lines and the *EM* distribution averages the information at each temperature coming from the lines forming around that temperature. Therefore, we may find significant discrepancies between the two solutions if there exist systematic differences between the line emissivity functions in the two databases and, in order to be relevant, these differences should affect several lines over a rather large interval of temperature. In practice, though most of the fluxes of Fe XVIII lines turn out to be systematically underestimated with the $EM(T)$ reconstructed using the CHIANTI database (see lower panel in Fig. 6), suggesting possible uncertainties in their emissivities, this occurrence did not affect the result appreciably, because some information on the amount of plasma at $\log T \sim 6.8$ (the temperature of formation of Fe XVIII) is also provided by the strength of the Fe XVII and Fe XIX lines included in the analysis.

As a further remark, we note that lines which largely disagree with others of the same ion are rejected in the selection phase; the disagreement may be due to errors in the emissivity functions, but also to the incompleteness of the database: in fact, one of the databases may ignore transitions giving important contributions to an observed spectral line (see in Table 3, for example, the lines at 10.10 Å, 10.36 Å, 15.09 Å, 15.87 Å, included in the analysis performed with APED, but not in that with CHIANTI).

5.2. Emission measure distribution vs. 3-T model solution

In Figs. 9 and 10 we compare the results obtained from the RGS and EPIC data. Figure 9 shows that the two hottest components
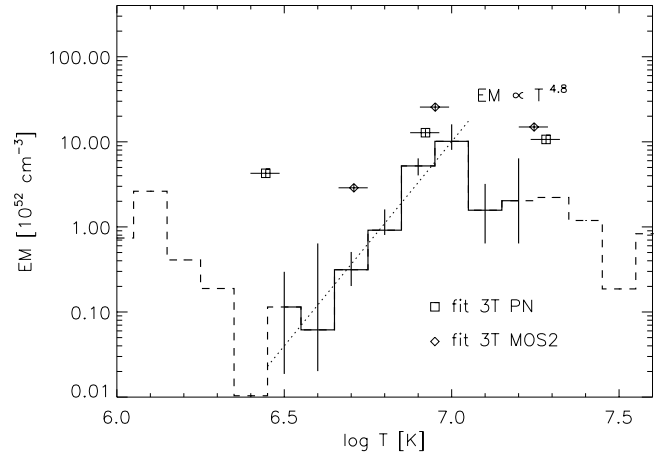

Fig. 9. RGS-derived *EM* distribution (histogram; dashed in poorly constrained regions) and EPIC best-fit 3-T solutions (squares for the pn and diamonds for the MOS2). The dotted line is the power-law $EM(T) \propto T^{4.8}$ best-fitting the ascending part of the distribution.
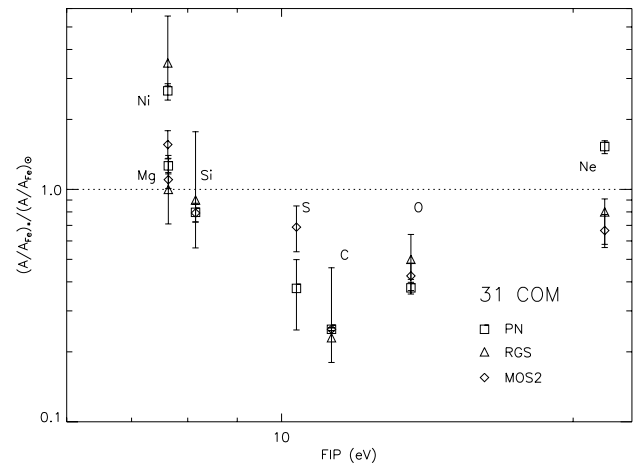

Fig. 10. Ratios between the elemental abundances of Fe and other elements, relative to the solar photospheric ratios (Grevesse et al. 1992), as a function of first ionization potential, derived from RGS (triangles), pn (squares) and MOS2 (diamonds).

of the pn and MOS2 3-T models agree; they are also consistent with the shape of the $EM(T)$, which peaks at $T \sim 10^7$ K and shows the presence of plasma at higher temperatures. On the contrary, the cool components are different; in particular, the pn best-fitting model provides a significant emission measure at $T \sim 10^{6.4}$ K, where the $EM(T)$ has its minimum.

In Fig. 10 we plot the elemental ratios $(A/A_{\rm Fe})_*/(A/A_{\rm Fe})_\odot$ derived from these three models vs. First Ionization Potential (FIP). We observe the largest discrepancies for Ni (the MOS2 value is significantly lower than the pn and RGS values) and Ne (the pn value is the highest), and we note a marginal inconsistency between the values for S (available from MOS2 and pn spectra only).

We have tested the capability of the 3-T models to describe the strength of individual emission lines with the ratios between observed and predicted fluxes shown in Fig. 11. By comparing this figure with the analogous one for the *EM* model (Fig. 6), we find that the best overall description of the
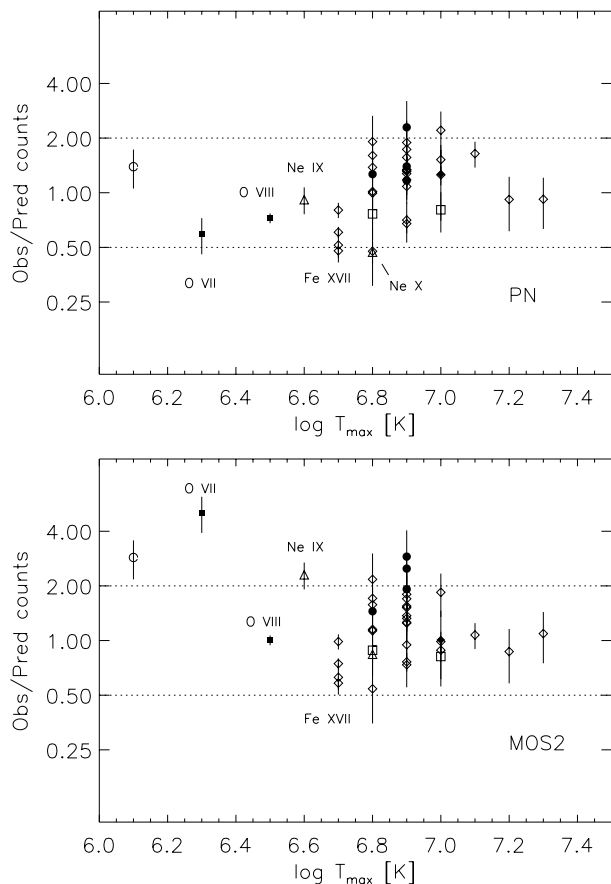
Fig. 11. Comparison between observed fluxes and the fluxes predicted with the pn 3-T model (upper panel) and MOS2 3-T model (lower panel), for lines used in the *EM* reconstruction; Fe: open diamonds, Ne: triangles, Mg: open squares, Si: filled diamond, Ni: filled circles, O: filled squares, C: open circle.

measured fluxes is provided by the RGS *EM* model, as expected; we note that this model underestimates the flux of the Ne IX resonance line, but we suspect that its measurement is not accurate, owing to the blend with Fe XIX (~13.52 Å). On the other hand, none of these models describes well the selected Ne IX 13.46 Å and Ne X 12.14 Å lines at the same time, supporting this hypothesis. The quality of the pn model seems to be comparable to that of the *EM(T)*, but this model over-predicts all the strong Fe XVII line fluxes, the O VII–VIII lines, as well as the Ne X line (whose measurement is more accurate than the Ne IX one). The main problems with the MOS2 model are instead the underprediction of the O VII and C VI lines, because of the too high temperature of the coolest component ($T_1 \sim 5$ MK), and of the Ni lines, as a consequence of the lower abundance derived for Ni by fitting the MOS2 spectrum with respect to the other cases.

Vice versa, by comparing the *EM* model spectrum (convolved with the pn and MOS2 responses) with the relative data of EPIC detectors, we have found systematic discrepancies at energies above ~15 Å.

It is evident that there is still some disagreement between the descriptions of the coronal plasma temperature structure, as independently derived from detailed emission measure analysis
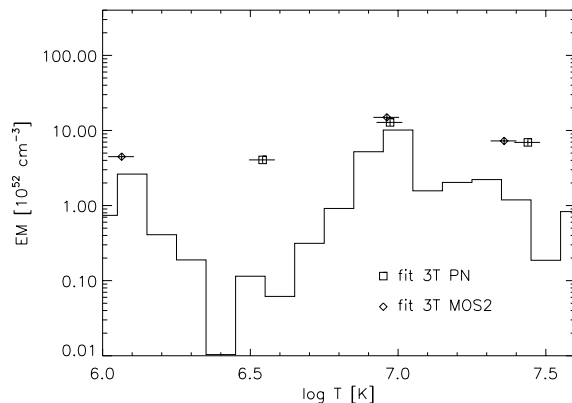

Fig. 12. 3-T solutions best-fitting the pn and MOS simulated spectra, generated with the same *EM(T)* (histogram) shown in figure.

of RGS spectra or from multi-T fitting of EPIC spectra. Such disagreements may be in part due to cross-calibrations uncertainties between the detectors, relevant at low energies and possibly not restricted to the MOS1 (see Appendix B).

Anyway, although 3-T models may suffice to describe EPIC spectra, we emphasize their roughness for a non-ambiguous determination of the thermal structure of coronal plasma, as described by *EM* models. To shed light on this aspect, we have generated X-ray spectra with the APED *EM(T)* model (see Fig. 5 and Table 4), using the same exposure times as in the pn and MOS observations (Table 1), convolved them with the current pn and MOS instrumental responses and applied poisso-nian statistics randomization to the relevant photon count numbers. We have then fitted these simulated pn and MOS spectra with absorbed 3-T models. Since the instrumental responses used to generate and fit each of the EPIC spectra are exactly the same, we can exclude any problem related to their unprecise knowledge, thus focusing just on the ability of pn- and MOS-like detectors in determining the thermal structure of coronal plasma. In brief, the most interesting result of this analysis is shown in Fig. 12: the two hottest components for the pn and the MOS models still agree with each others and are coherent with the *EM(T)*, but the cool components do not. This demonstrates that, even if we know exactly the instrumental responses of two detectors like the pn and MOS, the results of 3-T model fitting are inherently affected by some ambiguity about the description of the coronal thermal structure: in the example considered, i.e. a source whose thermal structure is described by the *EM(T)* shown in Fig. 12, the coolest components remain ill-determined.

As for the abundances, we consider the values obtained with the RGS the most accurate ones because they are based on individual line measurements, but it is worth noting that the abundances derived from the EPIC data (as well as those recovered by fitting the simulated spectra) differ at most by a factor 2 for some of the elements (see Ne and Ni in Fig. 10); hence, we conclude that 3-T model fitting of *XMM*/EPIC spectra of quality similar to those of 31 Com may suffice in determining the general behavior of the abundances vs. FIP in stellar coronae. On the other hand, a detailed analysis of *XMM* and *Chandra* observations of AB Dor (Sanz-Forcada et al. 2003) shows that

3-T models are not adequate to fit high-resolution X-ray spectra in a reliable way, and a line-based approach is preferable whenever feasible.

In the past years, several works have investigated the presence of a "First Ionization Potential (FIP) effect" in stellar coronae (Drake et al. 1997; Laming & Drake 1999; Bowyer et al. 2000), namely an enhancement of low-FIP elemental abundances in corona with respect to photospheric values, as proposed for the Sun (see, for a recent review, Feldman & Laming 2000). Most recently Audard et al. (2003) have studied a sample of RS CVn-like binary systems and have suggested that the FIP bias is correlated with the activity level, changing from a marked inverse FIP effect in highly active stars to a possible solar-like effect in low activity stars. We do not find evidence of either a clear FIP effect or an inverse FIP effect for the case of 31 Com (Fig. 10), but rather we observe a pattern of abundances vs. FIP with an initial decrease (with respect to solar photospheric values) down to a minimum value for carbon, followed by increasing abundances for elements with higher FIP (>11 eV), similar to the pattern found for the young active star AB Dor by Sanz-Forcada et al. (2003).

5.3. EM(T) and implications for coronal loops

We use the *EM* model distribution derived from RGS data to get clues on the loop population and on the properties of the quiescent coronal structures in 31 Com. Indeed, the light curve in Fig. 1 does not show any flare, thus supporting the hypothesis of an X-ray emission coming from stationary structures.

Owing to the low surface gravity of the star ($g_* \simeq 0.034\ g_\odot$) and to the high coronal temperatures, the pressure scale height H_p is of the order of the radius of 31 Com ($R_* \sim 6 \times 10^{11}$ cm): we obtain $H_p \sim 10^{11}$ cm for $T \sim 10^6$ K, and $H_p \sim 10^{12}$ cm for $T \sim 10^7$ K, where the lines contributing to the bulk of the observed X-ray emission form. We tentatively assume that the structures responsible for the observed emission have characteristic lengths smaller than the pressure scale height (see below). Under this hypothesis, the pressure is approximatively uniform inside each loop, implying that the emission measure distribution of a single loop depends only on its maximum temperature T_{max} (Maggio & Peres 1996), with a functional form $em(T) \propto T^\alpha$ for $T < T_{max}$. Considering that the $EM(T)$ of the whole stellar corona is the sum of the $em(T)$ of individual loops, following the approach by Peres et al. (2001) we interpret the constrained part of the $EM(T)$ as due to a population of loops, each of them having $em(T) \propto T^\alpha$, and whose distribution in T_{max} is negligible for $T_{max} < 10^7$ K. In fact, according to this model, the total $EM(T)$ would be proportional to T^α for $T < \min\{T_{max}\}$, and we observe that the emission measure distribution for 31 Com is approximatively a power-law for $10^{6.5}$ K $< T < 10^7$ K (Fig. 9). By means of a linear fitting over the latter temperature range, we have estimated the power-law slope $\alpha = 4.8 \pm 2.0$, which we assume as a characteristic of the emission measure distribution of individual loops. Note that loop models with constant cross-section and uniform heating would have $\alpha = 1.5$, which well describes the ascending slope of the emission measure distribution derived for the

solar corona as a whole (Orlando et al. 2000; Peres et al. 2000). The larger value we have obtained indicates that the dominant structures in the corona of 31 Com, having $T_{max} \sim 10^7$ K or higher, may be different from the solar ones[2]. Such structures are characterized by an excess of plasma emission measure at high temperatures, with respect to the solar case, that might be attained if the heating were concentrated at the loop footpoints, where the radiative losses are higher; in this way, the thermal conductive flux from the loop apex to the footpoints would play a minor role in the energy balance, thus flattening the temperature profile along the loop.

We emphasize that what just stated refers to the dominant population of coronal loops, at $T_{max} \sim 10^7$ K and higher; indeed, the derived $EM(T)$ suggests the presence of a cooler class of structures, at $T \sim 10^6$ K, but the available data do not allow us to obtain information about their α value.

Using a simplified coronal model, we can now show that the hypothesis of loops shorter than the pressure scale height is not at all restrictive. Let H be the height of the coronal loops with $T_{max} \sim 10^7$ K. The total volume of these structures is

$$V \simeq f \frac{4}{3} \pi \left[(R_* + H)^3 - R_*^3 \right] = f \frac{4}{3} \pi \chi(H, R_*) \tag{3}$$

where f is the volumetric filling factor. By referring to Fig. 9, we can estimate their total emission measure as:

$$EM_{tot} \simeq \sum_{T_k=10^{6.5}\ \mathrm{K}}^{T_k=10^7\ \mathrm{K}} EM_k \simeq 2 \times 10^{53}\ \mathrm{cm}^{-3}. \tag{4}$$

In order to get constraints in the isobaric plasma case, let us suppose first that the density is uniform along each loop; in this case,

$$EM_{tot} = n_e^2 V = n_e^2 f \frac{4}{3} \pi \chi(H, R_*) \tag{5}$$

hence

$$f = \frac{3\,EM_{tot}}{4\pi} \frac{1}{n_e^2} \frac{1}{\chi(H, R_*)}. \tag{6}$$

The curves f vs. n_e (with H as a parameter) are plotted in Fig. 13: if the loop density were uniform, heights larger than the pressure scale height (>10^{12} cm) would be compatible with the observed EM_{tot} only for unusually low densities or extremely small filling factors. Actually, since the pressure has to remain uniform along the loop, the density has to increase going from the loop apex to the footpoints; denoting the loop density at the apex again with n_e, Eq. (6) still holds with the < sign for the isobaric case:

$$f < \frac{3\,EM_{tot}}{4\pi} \frac{1}{n_e^2} \frac{1}{\chi(H, R_*)} \tag{7}$$

which reinforces the previous reasoning. Therefore, isobaric structures with $H < 10^{12}$ cm are possible for a large range of apex densities and filling factors.

From the analysis of the far-ultraviolet spectrum of 31 Com taken with the *Space Telescope Imaging Spectrograph*,

---

[2] Note that there is no mean of obtaining $EM(T) \propto T^5$ by summing up emission measure distributions whose ascending slope is $\alpha = 1.5$.
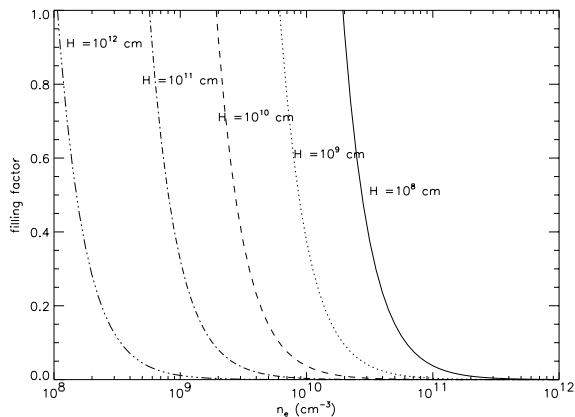
Fig. 13. Filling factor (f) as a function of the density (assumed to be uniform along the loop), for different values of the loop height. If n_e is the density at the apex of an isobaric loop, the curves have to be considered as upper limits for f.

Ayres et al. (2003) have found evidence for excess broadening, with respect to the thermal and instrumental ones, in the semipermitted subcoronal O V 1371 Å line and in the forbidden coronal Fe XXI 1354 Å line; in an analogous study of spectra taken with the *Far Ultraviolet Spectroscopic Explorer*, Redfield et al. (2003) have found evidence for anomalously large broadening of the Fe XVIII 974 Å coronal forbidden line. They interpret the large line widths[3] in terms of rotational broadening, which could indicate emission from highly extended coronal regions. In the following we examine the compatibility of this interpretation with our results.

First, we observe that, if we accept the hypothesis of rotational broadening and the values of the line widths measured by Ayres et al., the regions where the O V ($T \sim 2.5 \times 10^4$ K) and the Fe XXI ($T \sim 10^7$ K) lines form would be located respectively at $\sim 3 \times 10^{11}$ cm and $\sim 9 \times 10^{11}$ cm above the photosphere; the uncertainty on the width of the Fe XVIII 974 Å line measured by Redfield et al. is too large for deriving any further useful information.

Second, we have compared the observed fluxes of these Fe XXI and Fe XVIII lines with those predicted with the $EM(T)$ computed in the present work[4], and we have found excellent agreement for the Fe XXI line ($F = 1.03 \pm 0.06 \times 10^{-14}$ erg cm^{-2} s^{-1} observed vs. 1.04×10^{-14} predicted) and agreement within a factor 1.5 for the Fe XVIII line ($F = 0.70 \pm 0.07 \times 10^{-14}$ erg cm^{-2} s^{-1} observed vs. 0.46×10^{-14} predicted). So, the bulk of the $EM(T)$ describes well also these UV and far-UV lines, and we can deduce that all the plasma at $\sim 10^7$ K, i.e. at the top of the loops which dominate in the corona of 31 Com, is located at $\sim 10^{12}$ cm above the photosphere. Note that the height of these structures is comparable to the pressure scale height and hence they are approximatively in isobaric condition. Therefore, our results would be compatible with those of Ayres, Redfield and collaborators for apex densities and

filling factors constrained by the curve in Fig. 13 corresponding to $H = 10^{12}$ cm.

For the rest of our analysis we need the plasma density at the top of the hot ($T_{\max} \sim 10^7$ K) loops. From the *XMM-Newton* data, we have derived an estimate of the (average) plasma density only at $T \sim 2 \times 10^6$ K, namely at the temperature of formation of the O VII triplet (see Sect. 4.2.3). The related plasma pressure of $\sim$13 dyn cm^{-2} cannot be ascribed to the hot loops, but rather, more likely, to cooler loops with $T_{\max} \sim 10^6$ K, as suggested by the shape of the derived $EM(T)$ (Fig. 9). If we assume that indeed the corona of 31 Com is made of at least two classes of loops, and that loops with higher $T_{\max}$ have higher pressure, in analogy with the case of Capella (see Argiroffi et al. 2003) which is similar to 31 Com, then the extended structures with $H \sim 10^{12}$ cm and $T_{\max} \sim 10^7$ K should have pressure values larger than what derived from the O VII triplet. Given the uncertainty on the density measurement and assuming conservatively that the hot loops have $P_e > 1.5$ dyn cm^{-2}, i.e. the lowest value compatible with our results in Sect. 4.2.3, we obtain a lower limit for the apex density of these extended loops ($n_e > 5 \times 10^8$ cm^{-3}) and hence, from Fig. 13, a strict upper limit to the filling factor ($f < 4\%$), too small to be compatible with the absence of variability observed for this star.

Finally, the magnetic field needed to confine the plasma inside these long structures should be larger than $\sim$6 G. In particular, this value applies to the plasma at the loop apex, and a simple extrapolation to the photospheric level yield surface magnetic fields of the order of 10^3 G up to 10^4 G, depending on the assumed depth of a magnetic dipole configuration. Future observations and estimates of density and magnetic field could help in clarifying the issue of the coronal structures in Hertzsprung-gap giants which, in our opinion, remains still open.

6. Summary and conclusions

In this work we have analyzed *XMM-Newton* X-ray spectra of the high-luminous Hertzsprung-gap star 31 Com, focusing both on methodological issues and on the scientific aspect of deriving information about the magnetic coronal structures confining the emitting plasma.

At least for RGS spectra with photon counting statistics similar to that of the spectra of 31 Com, we have shown that: (i) flux measurements can be obtained from rebinned and co-added RGS spectra, using a Lorentzian as the line profile, provided the continuum level is estimated independently from the data; this method provides accurate line fluxes in a faster way than using individual RGS spectra and the detailed Line Spread Function for each spectral line; (ii) the emission measure distributions and the abundance sets obtained from RGS spectra with the two most up to date public emissivity databases currently available, i.e. APED and CHIANTI, are compatible, thus demonstrating the robustness of the method we have adopted and the reliability of our results.

By comparing 3-T models that fit the EPIC spectra and the emission measure distribution derived from RGS spectra, we have found some disagreements which have revealed

---

[3] Note that they made single-Gaussian fits to line profiles also in cases, such as the Fe XXI line, where the profile is flat-topped and decidedly non-Gaussian.

[4] The formation temperature of the O V 1371 Å line is outside the range of temperatures where the $EM(T)$ has been reconstructed.

cross-calibration uncertainties between the detectors onboard *XMM-Newton*, as well as the ambiguity of 3-T models in describing the thermal structure of coronal plasma. More precisely, we have found that (i) low-temperature components, as derived from pn and MOS spectra separately, may differ significantly; (ii) the metallicity obtained by fitting the MOS spectra is lower by a factor 2 than the values obtained with the pn and RGS data; (iii) it is difficult, if not impossible, to guess the shape of the emission measure distribution vs. temperature, as derived from the analysis of RGS spectra, starting from 3-T best-fit models. We stress that the above results (i) and (ii) should not be generalized naively to other cases of thermal emission line source, i.e. we are not claiming that they represent a systematic bias in the analysis results (for different outcomes, see, e.g., Güdel et al. 2001; Franciosini et al. 2002). We conclude that, at present, some care is needed to interpret the results of *XMM-Newton* observations, especially when these results are based on only one of the EPIC detectors. The calibration effort of the XMM instruments is still ongoing (Kirsch 2003) and hence we are confident that some inconsistencies among the various instruments will be likely resolved in the near future.

The $EM(T)$ of 31 Com peaks at $T \sim 10^7$ K and the ascending part of the distribution, for $10^{6.5}$ K $< T < 10^7$ K, is approximatively proportional to T^5. The steep slope of the $EM(T)$ confirm itself to be a characteristic of high-luminous stellar coronae, as already found in the case of Capella (Argiroffi et al. 2003), and not necessarily associated to active binary systems (in fact 31 Com is a putative single G-type giant). The corona of 31 Com appears to be dominated by a class of loops with maximum temperature $\sim 10^7$ K, having a steeper profile of the emission measure distribution vs. temperature with respect to the solar case; to explain the derived value of the total emission measure of such structures, relatively small loop lengths ($L < R_*$) are generally possible with filling factors strongly dependent on the plasma density, while extended structures necessarily imply very low apex densities ($n_e \sim 10^8$ cm^{-3}) or very small filling factors, hardly compatible with the absence of variability.

Appendix B: EPIC-RGS cross-calibration

We have found evidence of important uncertainties in the calibration at low energies at least for one of the two MOS detectors, as deduced from Fig. B.1 which shows the result of the simultaneous 3-T fitting of MOS spectra. Note that the MOS1 data are systematically under the model in the 15−20 Å region, while the MOS2 data are systematically above it, though the instrumental responses are practically the same (as evident from the closeness of the two model spectra).

We also show that the cross-calibration between MOS1 and RGS is not consistent in the region including the
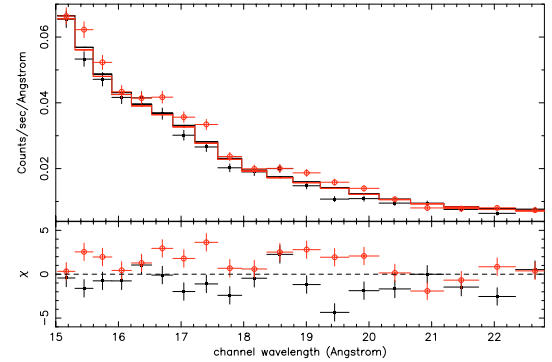

Fig. B.1. Particular of the MOS1 (filled squares) and MOS2 (open circles) observed spectra, with the relevant fitting spectra (solid lines). Note the closeness between the two predicted spectra and their systematic discrepancy with respect to the data (see the residuals) in the 15−20 Å region.
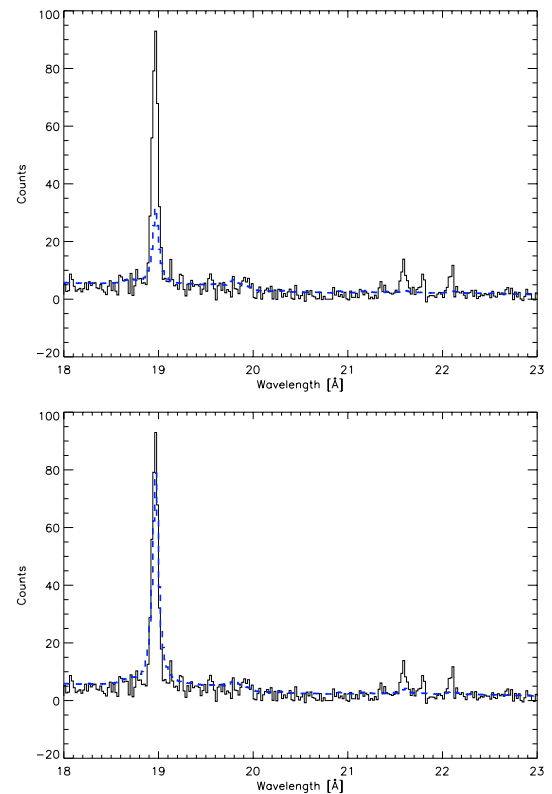

Fig. B.2. Comparison between the observed (solid line) and predicted (dashed line) RGS spectrum of 31 Com in the O VIII Ly α (18.97 Å) and O VII triplet (21.6 Å, 21.8 Å e 22.1 Å) region. *Upper panel*: MOS1 case. *Lower panel*: MOS2 case.

O VIII *Ly α* and the O VII triplet. Essentially, the MOS1 and MOS2 best-fit models (as stated in Sect. 4.1 the former is not statistically acceptable) differ significantly for the coolest temperature T_1 and the O abundance. In particular, these values for the MOS1 model ($T_1 \sim 7.2 \times 10^6$ K and $A_O/A_{O\odot} = 0.13 \pm 0.04$) imply that this model lacks appreciable contributions from the O lines, in fact it underpredicts the O VIII and O VII lines in RGS spectrum (upper panel in Fig. B.2); nevertheless, the model fits the data in this region (upper panel in Fig. B.3). On the contrary, the MOS2 model
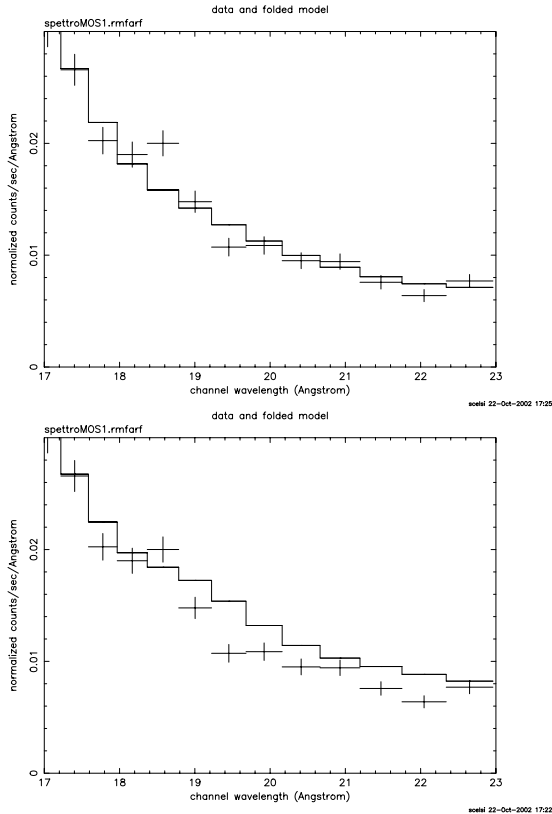
Fig. B.3. *Upper panel*: MOS1 data and best-fitting model. *Lower panel*: O lines are simulated by four monochromatic components with fluxes equal to the measured ones. Note the model overprediction, with respect to data, in the whole region containing the O VIII and O VII lines.

(Table 2) describes well the O VIII Ly α, underpredicting only the O VII triplet (Fig. 11 and lower panel in Fig. B.2).

To underline better the inconsistencies between the MOS and RGS detectors, we have fixed to zero the O abundance in the MOS1 model and we have simulated the O lines by adding four monochromatic components at the wavelengths of the O VIII Ly α and the O VII triplet, their fluxes equal to the measured ones in RGS spectrum. The result is shown in the lower panel of Fig. B.3: note the systematic overprediction of the model with respect to the data, which may indicate just an erroneous calibration between the MOS1 and the RGS detectors.

We have repeated the same analysis for the MOS2, but we did not observe this kind of disagreement. We explain this by noting that the MOS2 model describes well the strong O VIII Ly α and, owing to the spectral resolution (*FWHM* ~ 1 Å at these wavelengths), the far weaker O VII lines are not relevant for the comparison between model and data.

We conclude that the calibration problems are much more serious for the MOS1.

References

Argiroffi, C., Maggio, A., & Peres, G. 2003, A&A, 404, 1033
Audard, M., Güdel, M., Sres, A., Raassen, A. J. J., & Mewe, R. 2003, A&A, 398, 1137
Ayres, T. R., Brown, A., Harper, G. M., et al. 2003, ApJ, 583, 963
Ayres, T. R., Simon, T., Stern, R. A., et al. 1998, ApJ, 496, 428
Bowyer, S., Drake, J. J., & Vennes, S. 2000, ARA&A, 38, 231
de Medeiros, J. R., & Mayor, M. 1999, A&AS, 139, 433
den Herder, J. W., Brinkman, A. C., Kahn, S. M., et al. 2001, A&A, 365, L7
Dere, K. P., Landi, E., Mason, H. E., Monsignori Fossi, B. C., & Young, P. R. 1997, A&AS, 125, 149
Dere, K. P., Landi, E., Young, P. R., & Del Zanna, G. 2001, ApJS, 134, 331
Drake, J. J., Laming, J. M., & Widing, K. G. 1997, ApJ, 478, 403
Drake, J. J., Peres, G., Orlando, S., Laming, J. M., & Maggio, A. 2000, ApJ, 545, 1074
Feldman, U., & Laming, J. M. 2000, Phys. Scr., 61, 222
Franciosini, E., Sanz-Forcada, J., Maggio, A., & Pallavicini, R. 2002, in High Resolution X-ray Spectroscopy with XMM-Newton and Chandra
Güdel, M., Audard, M., Magee, H., et al. 2001, A&A, 365, L344
Gabriel, A. H., & Jordan, C. 1969, MNRAS, 145, 241
Gehrels, N. 1986, ApJ, 303, 336
Gondoin, P., Aschenbach, B., Erd, C., et al. 2000, in X-Ray and Gamma-Ray Instrumentation for Astronomy XI, ed. A. Kathryn, H. Flanagan, & O. Siegmund, Proc. SPIE, 4140, 1
Grevesse, N., Noels, A., & Sauval, A. J. 1992, in Coronal Streamers, Coronal Loops, and Coronal and Solar Wind Composition, 305
Guedel, M. 1997, ApJ, 480, L121
Houck, J. C., & Denicola, L. A. 2000, in Astronomical Data Analysis Software and Systems IX, ed. N. Manset, C. Veillet, & D. Crabtree, ASP Conf. Proc., 216, 591
Kashyap, V., & Drake, J. J. 1998, ApJ, 503, 450
Kashyap, V. L., & Drake, J. J. 2000, AAS/High Energy Astrophysics Division, 32, 0
Kirsch, M. 2003, XMM-SOC-CAL-TN-0018
Laming, J. M., & Drake, J. J. 1999, ApJ, 516, 324
Landi, E., Landini, M., Dere, K. P., Young, P. R., & Mason, H. E. 1999, A&AS, 135, 339
Maggio, A., & Peres, G. 1996, A&A, 306, 563
Maggio, A., Vaiana, G. S., Haisch, B. M., et al. 1990, ApJ, 348, 253
Mazzotta, P., Mazzitelli, G., Colafrancesco, S., & Vittorio, N. 1998, A&AS, 133, 403
Orlando, S., Peres, G., & Reale, F. 2000, ApJ, 528, 524
Paresce, F. 1984, AJ, 89, 1022
Peres, G., Orlando, S., Reale, F., & Rosner, R. 2001, ApJ, 563, 1045
Peres, G., Orlando, S., Reale, F., Rosner, R., & Hudson, H. 2000, ApJ, 528, 537
Perryman, M. A. C., Lindegren, L., Kovalevsky, J., et al. 1997, A&A, 323, L49
Piskunov, N., Wood, B. E., Linsky, J. L., Dempsey, R. C., & Ayres, T. R. 1997, ApJ, 474, 315
Pizzolato, N., Maggio, A., & Sciortino, S. 2000, A&A, 361, 614
Porquet, D., Mewe, R., Dubau, J., Raassen, A. J. J., & Kaastra, J. S. 2001, A&A, 376, 1113
Redfield, S., Ayres, T. R., Linsky, J. L., et al. 2003, ApJ, 585, 993
Sanz-Forcada, J., Brickhouse, N. S., & Dupree, A. K. 2002, ApJ, 570, 799
Sanz-Forcada, J., Maggio, A., & Micela, G. 2003, A&A, in press
Smith, R. K., Brickhouse, N. S., Liedahl, D. A., & Raymond, J. C. 2001, ApJ, 556, L91
Strüder, L., Briel, U., Dennerl, K., et al. 2001, A&A, 365, L18
Turner, M. J. L., Abbey, A., Arnaud, M., et al. 2001, A&A, 365, L27
Ueda, Y., Ishisaki, Y., Takahashi, T., Makishima, K., & Ohashi, T. 2001, ApJS, 133, 1
Young, P. R., Landi, E., & Thomas, R. J. 1998, A&A, 329, 291